ACS APPLIED MATERIALS & INTERFACES

Research Article

Cite This: ACS Appl. Mater. Interfaces 2020, 12, 2370−2379

www.acsami.org

Unraveling the Mechanism of Water-Mediated Sulfur Tolerance via Operando Surface-Enhanced Raman Spectroscopy

Jun Hyuk Kim,[†] Zhao-Ying Chern,[‡] Seonyoung Yoo,[†] Ben deGlee,[†] Jenghan Wang,[‡] and Meilin Liu*[,†]

[†]School of Materials Science and Engineering, Georgia Institute of Technology, Atlanta, Georgia 30332-0245, United States

[‡]Department of Chemistry, National Taiwan Normal University, 88, Section 4, Ting-Zhou Road, Taipei 11677, Taiwan, R.O.C.

Supporting Information

ABSTRACT: While several proton-conducting anode materials have shown excellent tolerance to sulfur poisoning, the mechanism is still unclear due largely to the inability to probe miniscule amounts of sulfur-containing species using conventional surface characterization techniques. Here we present our findings in unraveling the mechanism of water-mediated sulfur tolerance of a proton conductor under operating conditions empowered by surface-sensitive, operando surface-enhanced Raman spectroscopy (SERS) coupled with impedance spectroscopy. Contrary to the conventional view that surface-adsorbed sulfur is removed mainly by oxygen anions, it is found that $-SO_4$ groups on the surface of the proton conductor are converted to SO_2 by a water-mediated process, as confirmed by operando SERS analysis and density functional theory (DFT)-based calculations. The combination of operando SERS performed on a model electrode and theoretical computation offers an effective approach to investigate into complex mechanisms of electrode processes in various electrochemical systems, providing information vital to achieve the rational design of better electrode materials.

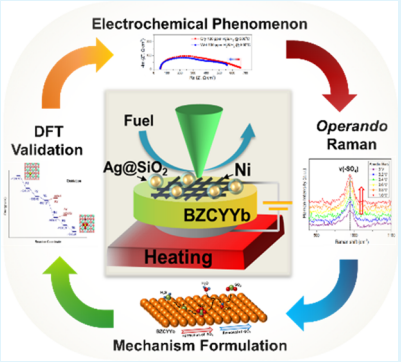

KEYWORDS: *fuel cell, sulfur poisoning, solid oxide fuel cell, anode, Raman spectroscopy*

INTRODUCTION

Solid oxide fuel cells (SOFCs) have the potential to be the cleanest and most efficient options for cost-effective conversion to electricity of a wide variety of fuels, from hydrogen to hydrocarbons, coal gas, and renewable fuels.[1−4] Analysis suggests that the replacement of today's engines, gas turbines, and power plants by SOFCs may be able to double the energy efficiency while dramatically reducing CO_2 emission.[5,6] However, small amounts of sulfur-containing contaminants may dramatically degrade the performance of the state-of-the-art cermet (ceramic−metal) anodes of SOFCs, and poor tolerance to fuel impurities severely limits the longevity of SOFCs and the market penetration of SOFC technology.[7−11] Since sulfur contaminants are commonly encountered in readily available fuels, such as natural gas and liquefied petroleum (LP),[8,10] the development of a contamination-tolerant anode is vital to fully achieve the fuel flexibility of SOFCs. While the kinetic activity of nickel (Ni), the most widely used metal in SOFC anode, is known to be inadequate for many practical fuels due likely to the formation of elemental sulfur (S*) that blocks active sites at the triple phase boundary (TPB),[9,10,12,13] Ni still has prospects to be one of the best anodes because of its exceptional catalytic activity toward H_2 oxidation, excellent electronic conductivity, and low cost. To date, extensive efforts have been devoted to the development of alternative ceramic counterpart of the cermet anode to preserve the aforementioned advantages of Ni while enhancing the sulfur tolerance of anode.

Over the past several years, important strides have been made in demonstrating effective sulfur tolerance utilizing proton-conducting oxides based on barium cerate−zirconate $Ba(Zr_{1-x}Ce_x)O_{3-\delta}$.[2,14,15] While sulfur poisoning on Ni is rigorously studied using ab initio atomistic calculations and in situ high-temperature Raman spectroscopy,[9,16−18] surface chemistry and structure of the ceramic phase of the cermet anodes are yet an important missing piece of the puzzle. Unraveling sulfur mitigation mechanism on a proton-conducting oxide of the cermet anode would be very important since many high-performance SOFCs are based on protonic ceramic-based anodes.[1,14,19−22] To date, however, no clear understanding has been reported, while many have speculated that a sulfur mitigation mechanism would be ascribed to the distinctive water adsorption capability of proton-conducting oxide.[2,10,14,23] The challenge mainly stems from the extremely low concentration of sulfur molecules [parts per million (ppm) level] and the inability to capture surface chemistry during the electrochemical reaction processes under typical fuel cell operating conditions.

Received: September 24, 2019
Accepted: December 17, 2019
Published: December 17, 2019

DOI: 10.1021/acsami.9b17294
ACS Appl. Mater. Interfaces 2020, 12, 2370−2379

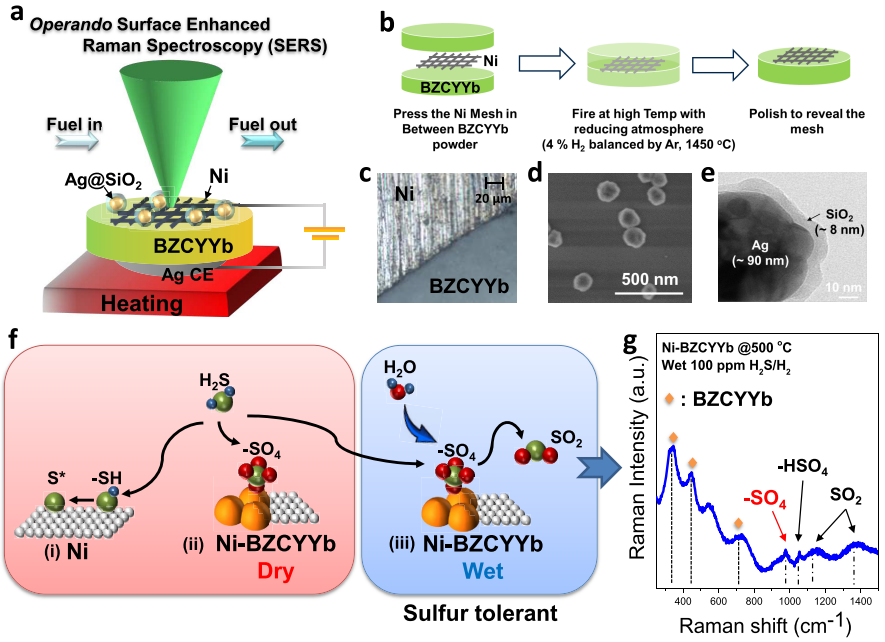

Figure 1. In situ/operando SERS platform. (a) Schematic of the in situ/operando SERS platform with a Ni−BZCYYb model electrode. (b) Schematic for the fabrication of patterned Ni electrode in BZCYYb powder through an embedded mesh method. (c) Optical microscope image of the surface of a model electrode showing Ni−BZCYYb interface. (d) Scanning electron microscopy (SEM) image of SERS NPs ($Ag@SiO_2$) on the surface of the model electrode. (e) TEM image of a SERS NP ($Ag@SiO_2$). (f) Schematics for sulfur transitions and the reaction mechanisms on (i) Ni, (ii) dry Ni−BZCYYb, and (iii) wet Ni−BZCYYb anode. (g) a typical SERS spectrum acquired in wet (3 vol % water vapor) H_2 fuel with 100 ppm H_2S at 500 °C.

One successful strategy to detect surface intermediates is employing surface-enhanced Raman spectroscopy (SERS) probes.[5,24−26] By utilizing electro-catalytically inert and thermally robust nanoprobes (NPs), Li et al. successfully identified $-CO_3$ functional groups on the surfaces of proton-conducting oxides, $BaZr_{0.9}Y_{0.1}O_{3-\delta}$ (BZY) and $BaZr_{0.1}Ce_{0.7}Y_{0.1}Yb_{0.1}O_{3-\delta}$ (BZCYYb), in investigation into the mechanism to coking tolerance.[27] It is found that surface-adsorbed water molecules play an important role in reducing or eliminating carbon deposition. While these studies have provided some valuable insights regarding the surface species that may critically affect the polarization resistance of an electrode, the detailed mechanism of electrode reactions is yet to be determined. To gain deeper insight into surface reaction mechanisms, it would be necessary to directly correlate electrode surface features under operating conditions with the electrochemical behavior of the electrode as determined using concurrent operando measurements such as electrochemical impedance spectroscopy (EIS).[28−31]

In this work, we probe the surface of Ni−BZCYYb model electrodes upon exposure to the ppm level of sulfur (H_2S) at elevated temperatures to acquire information relevant to sulfur mitigation mechanisms of this proton-conducting oxide. First, we directly observed $-SO_4$ surface functional group as a major species on the surface of BZCYYb; this became possible because SERS NPs significantly enhanced the detection limit of Raman spectroscopy. Further, the simultaneous measurement of Raman and impedance spectra allows us to build a quantitative relationship between Raman spectral features and the electrochemical behavior of the electrode. Second, the removal of $-SO_4$ by introducing water vapor was confirmed in time-resolved SERS, implying that water may play a critical role in sulfur removal from the surface of the proton-conducting oxide. This observation suggests that water adsorption may be equally effective as oxygen ion flux to remove adsorbed sulfur ($S^* + 2O^{2-} \rightarrow SO_2 + 4e^-$).[8,10] Third, density functional theory (DFT) calculations have helped us to explore possible elementary reaction sequences and the specific mechanism for sulfur removal.

EXPERIMENTAL SECTION

Fabrication of Model Electrodes. $BaZr_{0.1}Ce_{0.7}Y_{0.1}Yb_{0.1}O_{3-\delta}$ (BZCYYb) powder was fabricated by a solid-state reaction method. Stoichiometric amounts of high-purity barium carbonate, zirconium oxide, cerium oxide, ytterbium oxide, and yttrium oxide powders (all from Sigma-Aldrich Chemicals) were mixed by ball milling in ethanol for 48 h, followed by drying in an oven and calcination at 1100 °C in air for 10 h. The calcined powder was ball-milled again, followed by another calcination at 1100 °C in air for 10 h. Resulting X-ray diffraction (XRD) is shown in Figure S1a.

Patterned electrodes are fabricated by an embedded mesh method. To fabricate model electrodes with a well-defined nickel−electrolyte interface, BZCYYb powder was pressed into a pellet (300 MPa for 30 s) with nickel mesh (<1 cm piece) embedded. The pellets with a sandwich structure of BZCYYb/Ni mesh/BZCYYb are then sintered in 4% H_2/bal Ar at 1450 °C for 5 h to densify the electrolyte. After sintering, one side of the sintered sample was ground and polished with diamond suspensions to remove the excess electrolyte to expose the interface between the Ni and the electrolyte. A schematic of the fabrication is described in Figure 1b, and the resulting samples are characterized as illustrated in Figure S1. There are several reasons to use the BZCYYb/Ni mesh/BZCYYb trilayer samples in this study. First, when a BZCYYb/Ni mesh bilayer sample was used, the difference in shrinkage and mismatch in the thermal expansion of Ni and BZCYYb during sintering resulted in warping and/or delamination of the Ni−BZCYYb sample. In contrast, when symmetrical BZCYYb/Ni mesh/BZCYYb trilayer samples were sintered, those problems were eliminated, yielding flat samples. Second, Ba evaporation from BZCYYb surface during sintering at high

DOI: 10.1021/acsami.9b17294
ACS Appl. Mater. Interfaces 2020, 12, 2370−2379

temperatures was another problem, altering the surface chemistry and thus properties. Fabricating a trilayer sandwich structure and then grinding off the excess layer are an effective way to obtain a good Ni–BZCYYb interface (Ba evaporation became negligible) for the study.

In Situ/Operando Raman Spectroscopy. Raman spectra were acquired using a Renishaw RM 1000 spectromicroscopy system (~2 μm spot size). An air-cooled Ar laser (CVI Melles Griot) emitted at 514 nm was used for the excitation of Raman signal in this study with a total power of 10 mW. It is noted that high-power laser could generate local heating of the area under study and may potentially degrade SERS platform. To avoid this problem, the laser was defocused slightly from the focal point and the beam size was expanded to approximately 5 × 5 μm^2 (the beam size was 2 × 2 μm^2 when focused). The actual power density was therefore reduced by about 1 order of magnitude, from 10 mW (when fully focused) to ~1 mW (under the actual condition). The confocal slit was adjusted to 10 μm to minimize band-broadening effects. Spectra are collected as an extended scan with a rate of 77 s/spectrum (grating: 1800 lines/mm). To acquire a full spectrum, the total time needed was approximately ~600 s. A Harrick environmental chamber was used for in situ/operando Raman tests.[5,13,32] An in situ time-resolved study was conducted by placing the laser spot on the same location. To perform operando Raman spectroscopy study, the Ni–BZCYYb side was connected as the working electrode (WE) and the other side is brush-painted with a Ag paste to perform as the counter electrode (CE). As a control, a Ag–Ag symmetric cell with BZCYYb electrolyte of the same thickness was also tested (Figures S13 and S14). Impedance spectra were acquired using a Solartron SI 1255 HF frequency response analyzer interfaced with an EG&G PAR potentiostat model 273A with an alternating current (AC) amplitude of 10 mV in the frequency range from 100 kHz to 0.01 Hz. Gases (4% H_2/bal Ar, H_2, Ar, 100 ppm H_2S/H_2, UHP grade, Airgas) were metered with mass flow controllers and introduced into the chamber. To introduce 3 vol % water into the gas, a room-temperature bubbler was used. To ensure H_2S does not dissolve in water, 100 ppm of H_2S/H_2 gas was mixed after Ar flowed through the bubbler.

Fabrication of SERS Nanoprobes (NPs). The detailed fabrication method of SERS NPs is as described in our previous work.[24] The Ag NP seeds are fabricated (Figure S2a, left) as follows: 0.75 g of poly(vinylpyrrolidone) (PVP, M_w = ~55 000 g/mol) was dissolved in 3 mL of ethylene glycol (EG, 99.8%) and then mixed with 0.25 g of $AgNO_3$. The resulting solution was kept at 120 °C for 1 h under vigorous stirring. Afterward, 20 mL of ethanol was added to form a homogeneous Ag colloidal suspension. The application of SiO_2 shell is done by adding 1 mL of concentrated NH_4OH into the Ag suspension, and then, 0.3 mL of tetraethyl orthosilicate (TEOS) was introduced, after letting set for 1 h. The fabricated Ag@SiO_2 nanoparticles were extracted from the colloidal solution by repeated centrifugation at 6000 rpm with ethanol and deionized (D.I.) water (Figure S2a, right). Encapsulation of SiO_2 brought a slight shift in extinction profiles (Figure S2b). The enhancement in the Raman intensity of fabricated NPs is tested with diluted rhodamine solutions as shown in Figure S2c. Spectra of BZCYYb are compared before and after the deposition of SERS nanoprobes (NPs), and the results are shown in Figure S1b.

Computational Details. The density functional theory (DFT) calculations were performed using Vienna ab initio simulation package (VASP).[33−35] The computational method employed the generalized gradient approximation[36] with the Perdew–Wang 1991 formulation[37] for the exchange–correlation function, GGA-PW91, with the projector-augmented wave (PAW) method[38,39] that the cost-effective pseudopotential was utilized for core electron–ion interaction. The cutoff kinetic energy of the plane-wave basis for the valance electrons was set at 600 eV. The Brillouin-zone (BZ) integration was examined in the reciprocal space and sampled by the Monkhorst–Pack scheme[40] at a 0.05 × 2 (1/Å) interval. $BaZrO_3$ surface was constructed by nine (3 × 3) metal layers containing a total of 135 atoms, in which the bottom two layers were fixed at the optimized crystal lattice and the top seven layers were free to relax, to simulate the BZCYYb electrolyte; dopants of Y and Yb played an important role in creating oxygen vacancy and showed small energetic difference. The energetic and gradient convergences of 1×10^{-4} and 1×10^{-2} eV, respectively, were applied for the structural optimization and reaction energy (ΔE) calculation for each step. The Gibbs free energy (ΔG) for the overall process was further examined by including the thermodynamic corrections of bias voltage (V_{bias}) and gas species pressures on the computed ΔE. The transition states were located by the nudged elastic band (NEB) method at the same convergence criteria for the reaction barrier (E_a) calculation.

RESULTS AND DISCUSSION

Construction of In Situ / Operando SERS Platform. From a practical point of view, it is essential to incorporate pores into the anode to facilitate mass transport of fuels. In addition, the electronically conductive phase should be well dispersed with the ionic conductor to maximize the active TPB density. However, it is challenging to gain a fundamental understanding of the intrinsic properties of an electrode with conventional porosity since it is difficult to separate the intrinsic properties of the electrode material from the effect of microstructure, morphology, and surface chemistry on electrode performance. More importantly, the active TPBs in a porous cermet electrode are inaccessible to the probing laser of Raman spectrometer since only the TPBs located at or near the electrode–electrolyte interface are electrochemically active (and thus blocked by the porous electrode). Therefore, to gain a critical understanding of the intrinsic properties of Ni–BZCYYb anodes, we have devised a model cell through embedded mesh method (Figure 1a–e; see the supporting experimental procedures for fabrication details and additional characterizations are shown in Figure S1).[26,41] While the typical configuration of a porous cermet electrode complicates on identifying reactions happening on each material (ceramic or metal), the model electrode with well-established TPBs allows us to directly probe the surface of Ni, the ceramic phase, or the Ni-ceramic interface of the cermet anode. The open architecture of the model cell with patterned anode allows operando Raman spectroscopy in parallel to the electrochemical testing.

Although sulfur contaminants can be found in various forms such as H_2S, R-SH, CS_2, and COS, they are mostly converted to H_2S under reducing atmospheres of the anode.[10,14] Therefore, hydrogen with 100 ppm H_2S (i.e., 100 ppm H_2S/H_2) is chosen as the sulfur-contaminated fuel. Since the concentration of the sulfur contaminant in the atmosphere is in the ppm level, the key reaction intermediates associated with sulfur poisoning may be in trace amount on the electrode surface; thus, highly sensitive techniques are required to detect the surface species. Accordingly, even though a surface adsorbate may have Raman active vibrational mode, ordinary Raman spectroscopy may yield insufficient information.[42] Furthermore, high-temperature in situ/operando Raman spectroscopy poses a particular challenge of low signal-to-noise ratios, attributed to an increased visible radiation from the heated sample and increased variability of Raman modes at elevated temperature. Although SERS technique with sputtered nanoislands of Ag showed promise as applied to ex situ characterizations,[42] applying Ag nanoparticles to an in situ study introduces two new complications. First, silver itself can be catalytically active; silver nanoparticles may affect the electrochemical performance measurements and confound the reaction mechanism study. Second, silver nanoparticles are not stable at elevated temperatures and tend to coarsen into larger particles that have weaker localized surface plasmon resonance

DOI: 10.1021/acsami.9b17294
ACS Appl. Mater. Interfaces 2020, 12, 2370−2379

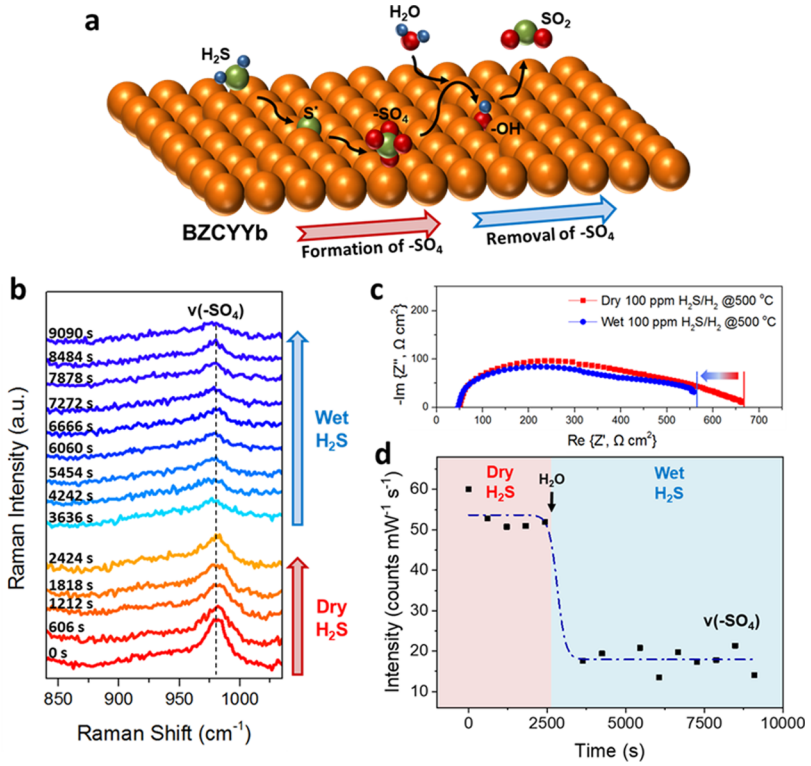

Figure 2. Investigation into water-mediated sulfur removal from BZCYYb. (a) Schematics for $-SO_4$ formation and water-mediated $-SO_4$ removal on a proton-conducting oxide, BZCYYb. (b) Time-resolved SERS analysis of a Ni−BZCYYb model electrode as the fuel was changed from dry to wet 100 ppm H_2S/H_2 at 500 °C. Laser was focused on BZCYYb. (c) Impedance spectra of the Ni−BZCYYb model electrode when exposed to dry and wet 100 ppm H_2S/H_2 at 500 °C. (d) Integrated intensities of the key peaks corresponding to $-SO_4$ of the Raman spectra shown in (b) as a function of time when 3 vol % water was introduced.

(LSPR) effects, which results in very small enhancement of the Raman scattering. Therefore, an inert shell is needed to restrain the catalytic activity of Ag and to prevent nanoparticle coarsening. To overcome aforementioned issues, we employed electro-catalytically inert and thermally robust Ag@SiO_2 (silver core with a silica shell) nanoparticles as shell-isolated nanoparticles enhanced Raman spectroscopy[43−45] (SHINERS) on model cell (Figures 1d,e and S2), which showed promising LSPR effect at temperatures up to 500 °C in our previous studies.[5,24,26] Fabricated BZCYYb has pure perovskite phase (confirmed by XRD), and in situ SERS measurements of the Ni−BZCYYb model electrode were performed to track the changes in surface composition with temperature in reducing atmosphere (1:1 = H_2/Ar) (Figure S1c). In the temperature-dependent Raman spectra, no major composition change was observed, while a slight thermal shift of the BZCYYb band was observed [doublet ∼350 cm^{-1} (v_1, v_2), ∼430 cm^{-1} (v_3)].[2,46] Thus, we have constructed anoperando SERS platform for investigation into the surface chemistry of Ni−BZCYYb model electrode under realistic fuel cell operating conditions containing sulfur-contained atmospheres.

Water-Mediated Removal of Sulfur on a Proton-Conducting Oxide. The principal evidence for the active role of BZCYYb in sulfur mitigation mechanism is the evoluation of Raman spectra as the partial pressure of water vapor in the fuel was changed (Figure 2). As seen in Figure 2b, when dry 100 ppm H_2S/H_2 was introduced to the model electrode at 500 °C, a band of sulfate [v($-SO_4$), 980 cm^{-1}][47−50] appeared quickly, an indication of sulfur adsorption and oxidation on BZCYYb surface. DFT calculations were used to guide the assignment of Raman peaks, and some of the vibrational frequencies of sulfur-containing species are listed in Table S3 (please see Figure S15, and the animations are also available in Videos S3−S9). According to Bartholomew et al., the toxicity of the sulfur-containing species depends on how many electron pairs are available to interact with the metal; therefore, their toxicity decreases as follows: H_2S > SO_2 > $-SO_4$.[51] Hence, it suggests that the formation of $-SO_4$ on BZCYYb can be advantageous to minimize the effect of sulfur poisoning of Ni surfaces. In the absence of water vapor in the fuel, however, $-SO_4$ remains on the surface [S_{dry} (standard deviation) = 3.86]. When the dry fuel gas was switched to a wet one (3 vol % H_2O + 100 ppm H_2S/H_2), v($-SO_4$) at 980 cm^{-1} quickly disappeared, as reflected in the integrated peak intensity of v($-SO_4$) over time [Figure 2d; S_{wet} (standard deviation) = 2.75]. Additionally, the peaks corresponding to SO_2,v(SO_2), appeared at 520, 1147, and 1334 cm^{-1} (Figures 1g, S3, and S4),[52] due likely to steam reforming of H_2S[14,53,54] The Raman analysis suggests that H_2O facilitates $-SO_4$ removal from the BZCYYb surface, which is supported by the time-resolved Raman observation of H_2O adsorption band (3580 cm^{-1}) and the formation of −OH (∼3300 cm^{-1}) groups on BZCYYb.[55] Thus, it seems that water plays a vital role in enhancing sulfur tolerance, as Yang et al. suggested earlier (Figure S5).[2,10] Moreover, Duan et al. illustrated remarkable sulfur resistance of $BaZr_{0.8}Y_{0.2}O_{3-\delta}$ (BZY20) and the role of dissociative water adsorption on proton-conducting oxide in improving sulfur tolerance.[14,56]

Although Raman spectroscopy is not a quantitative analysis technique, the amount of $-SO_4$ on the surface was estimated using pure $BaSO_4$ as a calibration sample under identical conditions for Raman analysis. The $BaSO_4$ sample had the same physical dimensions as the Ni−BZCYYb model electrode

DOI: 10.1021/acsami.9b17294
ACS Appl. Mater. Interfaces 2020, 12, 2370−2379

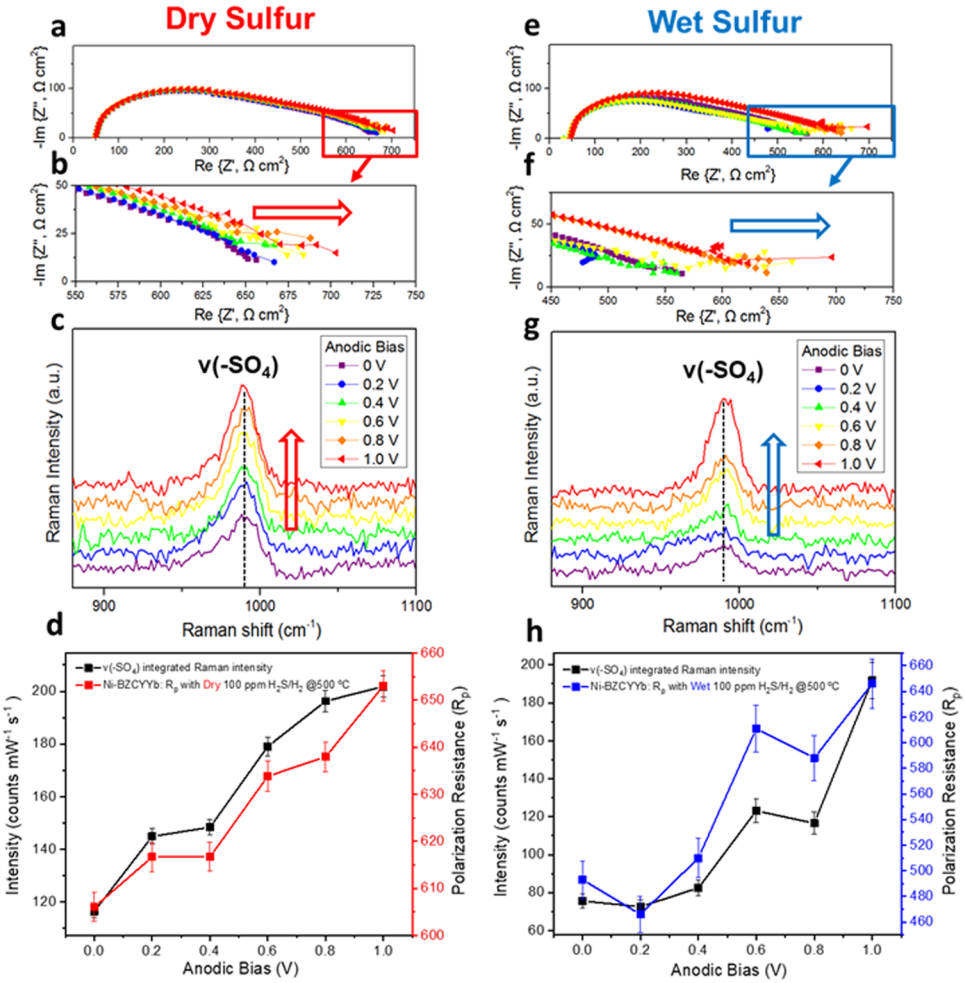

Figure 3. Quantitative analysis of concurrent Raman and impedance spectra. (a, b, e, f) Impedance spectra of a Ni−BZCYYb model electrode under (a) dry and (e) wet 100 ppm H_2S/H_2 at 500 °C. The anodic bias was changed from 0 to 1.0 V. (b, f) closer views of the low-frequency EIS data for easy comparison. (c, g) Operando Raman spectroscopic evolution of Ni−BZCYYb model electrode under (c) dry and (g) wet 100 ppm H_2S/H_2 at 500 °C under the influence of an applied anodic bias. Raman acquisitions are performed simultaneously with impedance spectroscopy at an interval of 0.2 V. (d, h) Quantitative correlation between key features, $v(-SO_4)$, of operando Raman spectra, and R_p of the model electrode under (d) dry and (h) wet 100 ppm H_2S/H_2 at 500 °C.

and was decorated with an equivalent amount of SERS NPs. The Raman measurements were performed under identical conditions as for the model anode (Figure S6). If the surface of the pure $BaSO_4$ sample is 100% covered by $-SO_4$, the surface of the BZCYYb in dry 100 ppm H_2S/H_2 has ∼0.6 % of $-SO_4$ surface coverage (estimated from the integrated area of the peak with a bandwidth of 20 cm^{-1}), which was reduced to ∼0.2% when 3% water vapor was introduced, indicating that 2/3 of the $-SO_4$ was removed from the BZCYYb surface.

This result is consistent with the EIS measurements under the same conditions in dry and wet 100 ppm H_2S/H_2 (Figure 2c). The polarization resistance (R_p) was higher in dry 100 ppm H_2S/H_2 ((more $-SO_4$ formation), but was reduced when water was introduced to the system ($-SO_4$ removal). The results support the hypothesis that $-SO_4$ is the major surface functional group that contributes most to an increase in polarization of the electrode under a sulfur-contained atmosphere. This result is also consistent with the R_p measurement reported by Yang et al. that BZCYYb anodes show no R_p increase when exposed to wet H_2 with small amount of sulfur (20 ppm H_2S/H_2).[2]

In addtion, Ni surface is also analyzed in both dry and wet 100 ppm H_2S/H_2 atmospheres at 500 °C, and the SERS evolution is shown in Figure S7. Since we observe −SH on Ni, which was also predicted from DFT calculations,[10,18] it is very plausible that H_2S preferentially cracked on Ni first and the sulfur moved to BZCYYb to form $-SO_4$. The R_p of the electrode seems to be dependent largely on the TPB area [where the ceramic phase (BZCYYb) is near to Ni (within 20 μm)], rather than the metal phase alone (Ni) of the cell. This suggests that the major polarization arises from an interface between Ni and BZCYYb. While it is known that sulfur coverage of Ni is mainly blamed for malicious poisoning effect, to enhance sulfur tolerance of SOFC anodes, the ceramic phase should act as a sulfur removal catalyst. Therefore, the ideal ceramic catalyst should have the capability to attract sulfur in order to protect Ni and, at the same time, should possess catalytic activity to remove sulfur from the surface. In this aspect, $Ba(Ce_{1-x}Zr_x)O_3$-based ceramics show a better tendency to react with H_2S , as confirmed by ab initio thermodynamic studies.[17,57] Moreover, it seems that sulfur tolerance of protonic ceramics is enhanced when water adsorption takes place. It should be noted that the active

DOI: 10.1021/acsami.9b17294
ACS Appl. Mater. Interfaces 2020, 12, 2370−2379

sites of cermet model anodes may not be confined only to the metal−ceramic interface but also extended to the two-phase boundaries (2PB) between ceramic and gas.[58] Overall, it involves $-SO_4$ development on proton-conducting oxide and subsequent water-mediated $-SO_4$ removal.

Quantitative Analysis of Raman Spectra and Electrode Polarization. To further verify our hypothesis that $-SO_4$ is the major functional group that results in the increase in in electrode polarization resistance (R_p), we designed additional operando Raman spectroscopy studies in order to directly correlate Raman results with electrochemical results, providing information for validation of electrode degradation mechanism. A combination of different techniques will help us to synthesize a predictive model. According to our previous discussions, sulfur transitions on BZCYYb surface involve two reactions: (1) $-SO_4$ formation and (2) $-SO_4$ removal.

The formation of $-SO_4$ (eq 1) could be hypothesized as follows

$$H_2S_{(g)} + 6O^{2-} \rightarrow 2OH^- + SO_4^{2-} + 8e^- \quad (1)$$

Since an applied anodic bias will draw electrons from the anode to external circuit, it is expected to facilitate $-SO_4$ formation on the anode. If the accumulation of $-SO_4$ functional groups increases the resistance to electrode reactions, an increase in anodic bias will lead to an increase in R_p of the model electrode.

When the anodic bias was varied from 0 to 1.0 V, the Raman band corresponding to $\nu(-SO_4)$ changed accordingly [dry 100 ppm H_2S/H_2; Figure 3c]. It is noted that the intensity of the $\nu(-SO_4)$ band increased with the magnitude of the anodic bias applied to the cell, implying that the anodic bias drives forward reaction (1). Concurrent measurement of EIS shows an increase in R_p accordingly (Figure 3a,b). Therefore, the evolution of the Raman band of $-SO_4$ is an indication of the surface reaction induced by sulfur poisoning.

Water-mediated sulfur removal (eq 2) in the presence of water (or in a wet atmosphere) can be expresed as follows

$$SO_4^{2-} + 2H_2O_{(g)} + 2e^- \rightarrow 4OH^- + SO_{2(g)} \quad (2)$$

Since electrons are required for this reaction, an applied anodic bias will slow down sulfur removal, implying less sulfur tolerance at high overpotential in the presence of water. To validate this, we performed operando Raman measurements in a wet atmosphere. When the anodic bias was varied from 0 to 1.0 V, the intensity of $\nu(-SO_4)$ and R_p of the model electrode quickly increased, suggesting that at high overpotential the bias effect can overwhelm the chemical effect of H_2O (Figure 3e−g).

The values of vibrational properties as a function of electrochemical operation can be considered as a semi-quantitative indication of surface functional group evolution induced by sulfur adsorption on the electrode surface. To quantify the effect, the intensity of the peak , $\nu(-SO_4)$ on BZCYYb sample was integrated with a bandwidth of 20 cm^{-1}. Figure 3d and 3h show the quantitative correlation between R_p and integrated peak intensity of $\nu(-SO_4)$. Whether it is in dry or wet atmosphere, it is clear that R_p of the cell is well corelated with the integrated intensity of $\nu(-SO_4)$ on the surface. Wet sulfur atmosphere shows much less R_p and $\nu(-SO_4)$ intensity in moderate anodic bias regime (0−0.4 V), suggesting that a water-mediating sulfur mitigation mechanism is operative as observed in long-term electrochemical performance studies.[2,14]

Mechanistic Assessment via Density Functional Theory. In addition to probing surface chemistry using Raman spectroscopic analysis, we further utilized DFT calculations for elaborating the mechanisms at the molecular level for eqs 1 and 2. To simplify the DFT simulation of BZCYYb, we started with undoped $BaZrO_3$ as a simplified DFT model in the beginning (Figures S8−S10); however, the energetics of Y- and Yb-doped $BaZrO_3$ were also considered in the subsequent analysis (Figures S11 and S12; Tables S1 and S2). Reaction 1 corresponds to the eight-electron oxidation process, starting from $H_2S_{(g)}$ to the subsequent formation of $SO_{4(b)}^{2-}$ along with $OH_{(b)}^-$ on the $BaZrO_3$ [the subscripts (g) and (b) indicate the species in the gas phase and bulk, respectively]. Reaction 1 can be decomposed to the elementary steps of R1−R6, as listed in Table 1a and shown in the corresponding potential energy surface (PES) in Figure 4a. (The complete reaction processes are detailed in the animation in Video S1.) As stated in the reaction coordinates and Table 1a, each elementary sequence of reaction 1 displays high exothermicities with negligible activation energy barriers (E_a), proving that the overall oxidation process readily occurs (overall ΔE_{oxi} = −17.21 eV), as identified with Raman spectroscopy. It is also worth noting that the Y- and Yb-doped $BaZrO_3$ describe similar energetics (Y-doped ΔE_{oxi}: −17.46, Yb-doped ΔE_{oxi}: −16.85 eV), indicating that $-SO_4$ functional group formation is energetically favorable on proton-conducting oxides (Table S1).

The $SO_{4(b)}^{2-}$ removal reaction 2, by the formation of $SO_{2(g)}$ along with dissociative $OH_{(b)}^-$ formation (in the presence of water), is a reduction process involving two-electron transfer, and the oxidation state of sulfur changes from +6 (SO_4^{2-}) to +4 (SO_2). The particular reaction sequence is listed in Table 1b, including the elementary steps of R7−R13, and the corresponding PES for the steps is shown in Figure 4b (the complete reaction processes are detailed in the animation in

Table 1. Elementary Reaction Sequences for Sulfate Formation and Water-Mediated Sulfate Removal Process

(a)[a]

steps	ΔE (eV)	E_a (eV)
R1: $H_2S_{(g)} + O^{2-} \rightarrow H_2SO_{(b)}^{2-}$	−3.57	
R2: $H_2SO_{(b)}^{2-} + O_{(b)}^{2-} \rightarrow HSO_{(b)}^{2-} + HO_{(b)}^- + e^-$	−2.31	0.05
R3: $HSO_{(b)}^{2-} + O_{(b)}^{2-} \rightarrow SO_{(b)}^{2-} + HO_{(b)}^- + e^-$	−2.42	0.02
R4: $SO_{(b)}^{2-} + O_{(b)}^{2-} \rightarrow SO_{2(b)}^{2-} + 2e^-$	−4.64	0.13
R5: $SO_{2(b)}^{2-} + O_{(b)}^{2-} \rightarrow SO_{3(b)}^{2-} + 2e^-$	−2.23	0.56
R6: $SO_{3(b)}^{2-} + O_{(b)}^{2-} \rightarrow SO_{4(b)}^{2-} + 2e^-$	−2.04	0.58

(b)[b]

steps	ΔE (eV)	E_a (eV)
R7: $SO_{4(b)}^{2-} + H_2O_{(g)} \rightarrow SO_{4(b)}^{2-} + H_2O_{(b)}$	−1.02	
R8: $SO_{4(b)}^{2-} + H_2O_{(b)} \rightarrow HSO_{4(b)}^- + OH_{(b)}^-$	−0.09	0.03
R9: $HSO_{4(b)}^- + 2e^- \rightarrow SO_{3(b)}^{2-} + OH_{(b)}^-$	1.32	1.81
R10: $SO_{3(b)}^{2-} + H_2O_{(g)} \rightarrow SO_{3(b)}^{2-} + H_2O_{(b)}$	−0.79	
R11: $SO_{3(b)}^{2-} + H_2O_{(b)} \rightarrow HSO_{3(b)}^- + OH_{(b)}^-$	0.72	1.33
R12: $HSO_{3(b)}^- \rightarrow SO_{2(b)} + OH_{(b)}^-$	0.20	1.01
R13: $SO_{2(b)} \rightarrow SO_{2(g)}$	0.44	

[a]The computed ΔE and E_a for the elementary steps of R1−R6 in the sulfate formation process from the $H_2S_{(g)}$ to the $SO_{4(b)}^{2-}$ on the $BaZrO_3$. The corresponding PES is plotted in Figure 4a. [b]The computed ΔE and E_a for the elementary steps of R7−R13 in the water-mediated sulfate removal process from the $SO_{4(b)}^{2-}$ to the $SO_{2(g)}$ on the $BaZrO_3$. The corresponding PES is plotted in Figure 4b.

DOI: 10.1021/acsami.9b17294
ACS Appl. Mater. Interfaces 2020, 12, 2370−2379

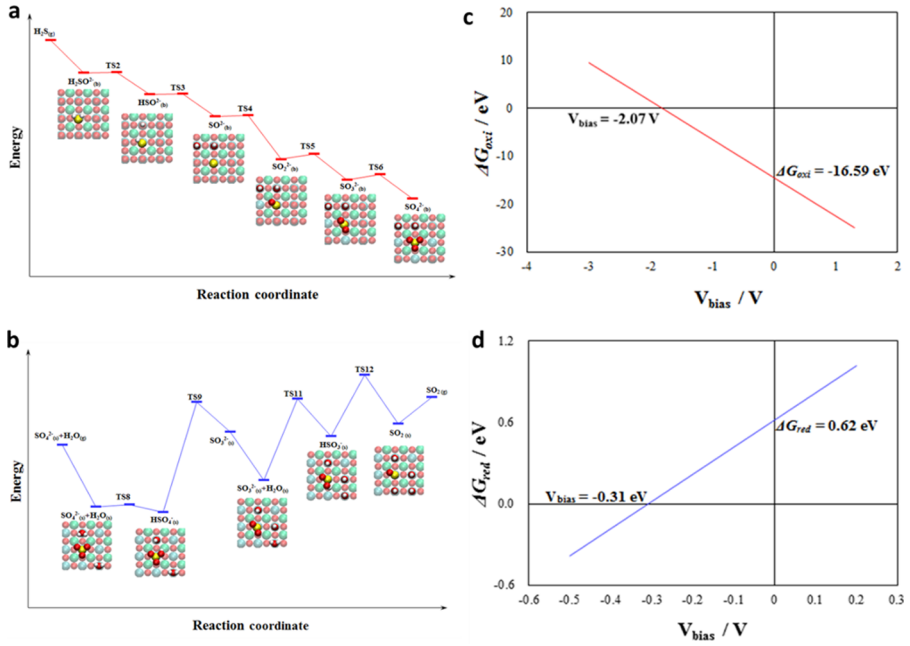

Figure 4. Mechanistic assessment via density functional theory. PES and the related structures of intermediate states in each step for (a) $-SO_4$ formation: $H_2S_{(g)} + 6O_{(b)}^{2-} \rightarrow SO_{4(b)}^{2-} + 2OH_{(b)}^{-} + 8e^{-}$ and (b) water-mediated $-SO_4$ removal process: $SO_{4(b)}^{2-} + 2H_2O_{(g)} + 2e^{-} \rightarrow SO_{2(g)} + 4OH_{(b)}^{-}$. The cyan, green, red, yellow, and white spheres are represented as Zr, Ba, O, S, and H atoms, respectively. The TSs indicate the transition states in the related step of R's. The computed Gibbs free energies in (c) $-SO_4$ formation, ΔG_{oxi}, and (d) water-mediated $-SO_4$ removal process, ΔG_{red}, process as functions of the anodic bias potential, V_{bias}.

Video S2). The reaction starts with the $H_2O_{(g)}$ adsorption, which has a barrierless behavior on the surface of the proton-conducting oxide (reaction R7). Then, H_2O dissociation happens with a negligible barrier to donate proton to $-SO_4$, forming $HSO_{4(b)}^{-} + OH_{(b)}^{-}$ (reaction R8). The formation of intermediate $-HSO_4$ is in good agreement with the Raman results (Figures 1g, S3, and S5), and the calculated result is comparable with the DFT calculation from Bandura et al., which they found that water dissociation can occur without a barrier on $BaZrO_3$.[56] Thus, the presence of H_2O vapor should be the limiting steps to determine sulfate removal reaction rate. $HSO_{4(b)}^{-}$, the protonated $SO_{4(b)}^{2-}$, can better cleave the strong S−O bond ($\Delta E/E_a$ = 1.32/1.81 eV), compared to those in the S−O bond cleavage in unprotonated $SO_{4(b)}^{2-}$ ($\Delta E/E_a$ = 2.04/2.62 eV) in the reversed step of R6. The second water adsorption (reaction R10) can provide additional proton source to protonate intermediate $SO_{3(b)}^{2-}$ species (reaction R11) to form $SO_{2(b)}$ (reaction R12). Finally, $SO_{2(b)}$ can desorb from the surface (reaction R13) with a moderate desorption energy (ΔE = 0.44 eV) to complete the sulfur removal process. The overall reduction process shows very low endothermicity (overall ΔE_{red} = 0.78 eV), which implies that the removal of $-SO_4$ can be practically achieved when thermodynamic properties are adjusted as seen in the Raman analysis. Please note that Yb doping further changes the spontaneity of the $-SO_4$ removal, as the overall ΔE_{red} is reduced to 0.64 eV, indicating that a beneficial sulfur-tolerant effect can be expected from Yb doping (Table S2). Overall, our DFT results demonstrate that surface-adsorbed sulfur can be removed through the formation of sulfate; however, the subsequent removal of $-SO_4$ requires $-OH/H_2O$.

To examine the bias-dependent $-SO_4$ accumulation behaviors, we further applied the thermodynamic corrections from anodic bias voltage to examine the Gibbs free energy and the corresponding spontaneity. The Gibbs free energy of sulfate formation reaction (ΔG_{oxi}) can be expressed as eq 3

$$\Delta G_{oxi} = \Delta E_{oxi} + RT \ln(p_o/pH_2S) - 8V_{bias} \quad (3)$$

where R is the ideal gas constant, T is the operation temperature at 500 °C (773 K), p_o is the standard pressure of 1 bar, pH_2S is the H_2S partial pressure of 100 ppm (10^{-4} bar), and $-8V_{bias}$ corresponds to the eight-electron oxidation process, where V_{bias} is the applied anodic bias voltage varied from 0 to 1.0 V. Analogously, the Gibbs free energy of sulfate removal reaction (ΔG_{red}) can be expressed as eq 4

$$\Delta G_{red} = \Delta E_{red} + RT \ln(pSO_2/(pH_2O)^2) + 2V_{bias} \quad (4)$$

where pSO_2 and pH_2O correspond to the partial pressures of the product (70 ppm, 7×10^{-5} bar) and reactant (0.03 bar), respectively, and $+2V_{bias}$ corresponds to the two-electron reduction process. The computed ΔG_{oxi} and ΔG_{red} as functions of V_{bias} are plotted in Figure 4c,d, respectively.

Figure 4c shows that ΔG_{oxi} decreases steeply as V_{bias} increases, attributable to the $-8V_{bias}$ term in ΔG_{oxi}. The result indicates that the eight-electron oxidation reaction favors $SO_{4(b)}^{2-}$ formation at higher V_{bias}, explaining the experimental observation that $\nu(SO_4^{2-})$ peak has larger intensity as higher anodic bias is applied on the cell. Figure 4d shows that ΔG_{red} increases slightly as V_{bias} increases, corresponding to the $+2V_{bias}$ term in the two-electron reduction process. The plot suggests that the spontaneity of water removal of $SO_{4(b)}^{2-}$ diminishes at higher V_{bias}, rationalizing the experimental observation that the intensity of $\nu(SO_4^{2-})$ drops at lower anodic bias in the presence of water. The Gibbs free-energy analysis satisfactorily explains the bias-driven $-SO_4$ accumulation observed in operando Raman spectroscopy (Figure 3), signifying that our mechanism formulation of water-mediated sulfur mitigation reaction is solid and rigorous. Comprehensive studies to

DOI: 10.1021/acsami.9b17294
ACS Appl. Mater. Interfaces 2020, 12, 2370−2379

observe the electrode surface, the structure of the interface, and the participating reactants are an essential step to develop sulfur-tolerant anode for SOFCs. Our detailed mechanistic understanding of the surface catalytic reaction can assist us to understand the dynamics of performance degradation, providing vital information to achieve the rational design of novel electrodes.

CONCLUSIONS

In summary, by performing surface-sensitive operando SERS on a Ni−BZCYYb model electrode exposed to a sulfur-containing fuel, we have investigated the reaction processes on the surface of the proton-conducting oxide (BZCYYb) under conditions similar to fuel cell operation. We found that $-SO_4$ is the key surface functional group on BZCYYb, which can be removed by a water-mediated process. Our direct operando observation and atomistic calculation confirm the crucial role of water in sulfur tolerance of the proton-conducting oxide. The strategy to remove elemental sulfur (S*) from anode surface by oxygen anion flux alone might be insufficient to achieve sulfur-tolerance. Rather, water-assisted sulfate reformation should be considered an alternative approach to achieving robust anode operation in sulfur-contained fuels. The new insight into the cause of performance degradation in SOFCs when exposed to sulfur can provide useful guidance to the development of a novel electrode with excellent durability against sulfur-contained fuels. Further, the developed methodology is applicable to the investigation into surface processes on other electrodes for related applications.

ASSOCIATED CONTENT

Supporting Information

The Supporting Information is available free of charge at https://pubs.acs.org/doi/10.1021/acsami.9b17294.

Additional physical, chemical, and electrical characterizations of BZCYYb model cells and SERS nanoparticles, and supporting Raman spectra (Figures S1−S7, S13, and S14); additional computational information (Figures S8−S12 and S15 and Tables S1−S3) (PDF)

Animation for oxidation (Video S1) (MP4)

Animation for reduction (Video S2) (MP4)

Animation for $-HSO_4$ vibration of −OH stretching at 3769 cm^{-1} (Video S3) (MP4)

Animation for $-HSO_4$ vibration of S═O stretching at 1248 cm^{-1} (Video S4) (MP4)

Animation for $-HSO_4$ vibration of S═O stretching at 1110 cm^{-1} (Video S5) (MP4)

Animation for $-HSO_4$ vibration of S═O stretching at 1050 cm^{-1} (Video S6) (MP4)

Animation for $-SO_4$ vibration of S═O stretching at 987 cm^{-1} (Video S7) (MP4)

Animation for SO_2 vibration of asymmetric S═O stretching at 1229 cm^{-1} (Video S8) (MP4)

Animation for SO_2 vibration of symmetric S═O stretching at 1038 cm^{-1} (Video S9) (MP4)

AUTHOR INFORMATION

Corresponding Author

*E-mail: meilin.liu@mse.gatech.edu.

ORCID

Jenghan Wang: 0000-0002-3465-4067

Meilin Liu: 0000-0002-6188-2372

Author Contributions

M.L. conceived and supervised the project. J.H.K. fabricated test cells and performed in situ/operando Raman spectroscopy analysis and electrochemical measurements. Z.-Y.C. and J.W. performed the DFT calculations. S.Y. and B.d. fabricated powder samples and performed XRD and microanalysis. J.H.K., B.d., and M.L. contributed to the writing of this paper.

Notes

The authors declare no competing financial interest.

ACKNOWLEDGMENTS

This work was supported by the U.S. Department of Energy (under award number DE-FE0031201), U.S. National Science Foundation (under award number DMR-1742828), Phillips 66, and agency of Ministry of Science and Technology, R.O.C (MOST 107-2113-M-003-008). This research used computational resources from Taiwan's National Center for High-performance Computing (NCHC).

REFERENCES

(1) Chen, Y.; deGlee, B.; Tang, Y.; Wang, Z.; Zhao, B.; Wei, Y.; Zhang, L.; Yoo, S.; Pei, K.; Kim, J. H.; Ding, Y.; Hu, P.; Tao, F. F.; Liu, M. A robust fuel cell operated on nearly dry methane at 500 °C enabled by synergistic thermal catalysis and electrocatalysis. *Nat. Energy* **2018**, 1042.

(2) Yang, L.; Wang, S.; Blinn, K.; Liu, M.; Liu, Z.; Cheng, Z.; Liu, M. Enhanced sulfur and coking tolerance of a mixed ion conductor for SOFCs: BaZr0. 1Ce0. 7Y0. 2−xYbxO3−δ. *Science* **2009**, *326*, 126−129.

(3) Liu, M.; Lynch, M. E.; Blinn, K.; Alamgir, F. M.; Choi, Y. Rational SOFC material design: new advances and tools. *Mater. Today* **2011**, *14*, 534−546.

(4) Yang, L.; Choi, Y.; Qin, W.; Chen, H.; Blinn, K.; Liu, M.; Liu, P.; Bai, J.; Tyson, T. A.; Liu, M. Promotion of water-mediated carbon removal by nanostructured barium oxide/nickel interfaces in solid oxide fuel cells. *Nat. Commun.* **2011**, *2*, No. 357.

(5) Chen, Y.; Yoo, S.; Choi, Y.; Kim, J. H.; Ding, Y.; Pei, K.; Murphy, R.; Zhang, Y.; Zhao, B.; Zhang, W.; Chen, H.; Chen, Y.; Yuan, W.; Yang, C.; Liu, M. A highly active, CO2-tolerant electrode for the oxygen reduction reaction. *Energy Environ. Sci.* **2018**, *11*, 2458−2466.

(6) Chen, Y.; Choi, Y.; Yoo, S.; Ding, Y.; Yan, R.; Pei, K.; Qu, C.; Zhang, L.; Chang, I.; Zhao, B.; et al. A Highly Efficient Multi-phase Catalyst Dramatically Enhances the Rate of Oxygen Reduction. *Joule* **2018**, 938.

(7) Riegraf, M.; Yurkiv, V.; Schiller, G.; Costa, R.; Latz, A.; Friedrich, K. A. The Influence of Sulfur Formation on Performance and Reforming Chemistry of SOFC Anodes Operating on Methane Containing Fuel. *J. Electrochem. Soc.* **2015**, *162*, F1324−F1332.

(8) Boldrin, P.; Ruiz-Trejo, E.; Mermelstein, J.; Bermúdez Menéndez, J. M.; Ramírez Reina, T.; Brandon, N. P. Strategies for carbon and sulfur tolerant solid oxide fuel cell materials, incorporating lessons from heterogeneous catalysis. *Chem. Rev.* **2016**, *116*, 13633−13684.

(9) Cheng, Z.; Liu, M. Characterization of sulfur poisoning of Ni−YSZ anodes for solid oxide fuel cells using in situ Raman microspectroscopy. *Solid State Ionics* **2007**, *178*, 925−935.

(10) Cheng, Z.; Wang, J.-H.; Choi, Y.; Yang, L.; Lin, M.; Liu, M. From Ni-YSZ to sulfur-tolerant anode materials for SOFCs: electrochemical behavior, in situ characterization, modeling, and future perspectives. *Energy Environ. Sci.* **2011**, *4*, 4380−4409.

(11) da Silva, A. L.; Heck, N. C. Thermodynamics of sulfur poisoning in solid oxide fuel cells revisited: the effect of H 2 S concentration, temperature, current density and fuel utilization. *J. Power Sources* **2015**, *296*, 92−101.

(12) Cheng, Z.; Abernathy, H.; Liu, M. Raman spectroscopy of nickel sulfide Ni3S2. *J. Phys. Chem. C* **2007**, *111*, 17997−18000.

DOI: 10.1021/acsami.9b17294
ACS Appl. Mater. Interfaces 2020, 12, 2370−2379

(13) Blinn, K. S.; Abernathy, H.; Li, X.; Liu, M.; Bottomley, L. A.; Liu, M. Raman spectroscopic monitoring of carbon deposition on hydrocarbon-fed solid oxide fuel cell anodes. *Energy Environ. Sci.* **2012**, *5*, 7913−7917.
(14) Duan, C.; Kee, R. J.; Zhu, H.; Karakaya, C.; Chen, Y.; Ricote, S.; Jarry, A.; Crumlin, E. J.; Hook, D.; Braun, R.; Sullivan, N. P.; O'Hayre, R. Highly durable, coking and sulfur tolerant, fuel-flexible protonic ceramic fuel cells. *Nature* **2018**, *557*, 217−222.
(15) Sengodan, S.; Liu, M.; Lim, T.-H.; Shin, J.; Liu, M.; Kim, G. Enhancing sulfur tolerance of a Ni-YSZ anode through BaZr0. 1Ce0.7Y0.1Yb0.1O3−δ infiltration. *J. Electrochem. Soc.* **2014**, *161*, F668−F673.
(16) Lee, K.; Song, C.; Janik, M. J. Ab initio thermodynamics examination of sulfur species present on Rh, Ni, and binary Rh−Ni surfaces under steam reforming reaction conditions. *Langmuir* **2012**, *28*, 5660−5668.
(17) Wang, J.-H.; Liu, M. Computational study of sulfur−nickel interactions: A new S−Ni phase diagram. *Electrochem. Commun.* **2007**, *9*, 2212−2217.
(18) Choi, Y. M.; Compson, C.; Lin, M. C.; Liu, M. A mechanistic study of H2S decomposition on Ni- and Cu-based anode surfaces in a solid oxide fuel cell. *Chem. Phys. Lett.* **2006**, *421*, 179−183.
(19) Choi, S.; Kucharczyk, C. J.; Liang, Y.; Zhang, X.; Takeuchi, I.; Ji, H.-I.; Haile, S. M. Exceptional power density and stability at intermediate temperatures in protonic ceramic fuel cells. *Nat. Energy* **2018**, 202.
(20) Chen, Y.; Yoo, S.; Pei, K.; Chen, D.; Zhang, L.; deGlee, B.; Murphy, R.; Zhao, B.; Zhang, Y.; Chen, Y.; Liu, M. An In Situ Formed, Dual-Phase Cathode with a Highly Active Catalyst Coating for Protonic Ceramic Fuel Cells. *Adv. Funct. Mater.* **2018**, *28*, No. 1704907.
(21) Duan, C.; Tong, J.; Shang, M.; Nikodemski, S.; Sanders, M.; Ricote, S.; Almansoori, A.; O'Hayre, R. Readily processed protonic ceramic fuel cells with high performance at low temperatures. *Science* **2015**, *349*, 1321.
(22) An, H.; Lee, H.-W.; Kim, B.-K.; Son, J.-W.; Yoon, K. J.; Kim, H.; Shin, D.; Ji, H.-I.; Lee, J.-H. A 5 × 5 cm2 protonic ceramic fuel cell with a power density of 1.3 W cm−2 at 600 °C. *Nat. Energy* **2018**, *3*, 870−875.
(23) Wang, F.; Wang, W.; Qu, J.; Zhong, Y.; Tade, M. O.; Shao, Z. Enhanced sulfur tolerance of nickel-based anodes for oxygen-ion conducting solid oxide fuel cells by incorporating a secondary water storing phase. *Environ. Sci. Technol.* **2014**, *48*, 12427−12434.
(24) Li, X.; Lee, J.-P.; Blinn, K. S.; Chen, D.; Yoo, S.; Kang, B.; Bottomley, L. A.; El-Sayed, M. A.; Park, S.; Liu, M. High-temperature surface enhanced Raman spectroscopy for in situ study of solid oxide fuel cell materials. *Energy Environ. Sci.* **2014**, *7*, 306−310.
(25) Stiles, P. L.; Dieringer, J. A.; Shah, N. C.; Van Duyne, R. P. Surface-Enhanced Raman Spectroscopy. *Annu. Rev. Anal. Chem.* **2008**, *1*, 601−626.
(26) Li, X.; Liu, M.; Lee, J.-p.; Ding, D.; Bottomley, L. A.; Park, S.; Liu, M. An operando surface enhanced Raman spectroscopy (SERS) study of carbon deposition on SOFC anodes. *Phys. Chem. Chem. Phys.* **2015**, *17*, 21112−21119.
(27) Li, X.; Liu, M.; Lai, S. Y.; Ding, D.; Gong, M.; Lee, J.-P.; Blinn, K. S.; Bu, Y.; Wang, Z.; Bottomley, L. A.; et al. In situ probing of the mechanisms of coking resistance on catalyst-modified anodes for solid oxide fuel cells. *Chem. Mater.* **2015**, *27*, 822−828.
(28) Catalysis as it goes. *Nat. Catal.* **2018**, *1* 165 166. DOI: 10.1038/s41929-018-0050-4.
(29) Chen, X.; Brasiliense, V.; Van Duyne, R. P. Operando Observation of Molecular-Scale Manipulation Using Electrochemical Tip-Enhanced Raman Spectroscopy. *J. Phys. Chem. C* **2018**, *122*, 24329−24333.
(30) Hackler, R. A.; McAnally, M. O.; Schatz, G. C.; Stair, P. C.; Van Duyne, R. P. Identification of dimeric methylalumina surface species during atomic layer deposition using operando surface-enhanced Raman spectroscopy. *J. Am. Chem. Soc.* **2017**, *139*, 2456−2463.
(31) Masango, S. S.; Hackler, R. A.; Henry, A.-I.; McAnally, M. O.; Schatz, G. C.; Stair, P. C.; Van Duyne, R. P. Probing the chemistry of alumina atomic layer deposition using operando surface-enhanced Raman spectroscopy. *J. Phys. Chem. C* **2016**, *120*, 3822−3833.
(32) Chen, Y.; Yoo, S.; Zhang, W.; Kim, J. H.; Zhou, Y.; Pei, K.; Kane, N.; Zhao, B.; Murphy, R.; Choi, Y.; Liu, M. Effective Promotion of Oxygen Reduction Reaction by in Situ Formation of Nano-structured Catalyst. *ACS Catal.* **2019**, 7137−7142.
(33) Kresse, G.; Furthmüller, J. Efficient iterative schemes for ab initio total-energy calculations using a plane-wave basis set. *Phys. Rev. B: Condens. Matter Mater. Phys.* **1996**, *54*, 11169−11186.
(34) Kresse, G.; Hafner, J. Ab initio molecular dynamics for liquid metals. *Phys. Rev. B: Condens. Matter Mater. Phys.* **1993**, *47*, 558−561.
(35) Kresse, G.; Hafner, J. Ab initio molecular-dynamics simulation of the liquid-metal-amorphous-semiconductor transition in germa-nium. *Phys. Rev. B: Condens. Matter Mater. Phys.* **1994**, *49*, 14251−14269.
(36) Ceperley, D. M.; Alder, B. J. Ground State of the Electron Gas by a Stochastic Method. *Phys. Rev. Lett.* **1980**, *45*, 566−569.
(37) Perdew, J. P.; Wang, Y. Accurate and simple analytic representation of the electron-gas correlation energy. *Phys. Rev. B: Condens. Matter Mater. Phys.* **1992**, *45*, 13244−13249.
(38) Blöchl, P. E. Projector augmented-wave method. *Phys. Rev. B: Condens. Matter Mater. Phys.* **1994**, *50*, 17953−17979.
(39) Kresse, G.; Joubert, D. From ultrasoft pseudopotentials to the projector augmented-wave method. *Phys. Rev. B: Condens. Matter Mater. Phys.* **1999**, *59*, 1758−1775.
(40) Monkhorst, H. J.; Pack, J. D. Special points for Brillouin-zone integrations. *Phys. Rev. B: Condens. Matter Mater. Phys.* **1976**, *13*, 5188−5192.
(41) Blinn, K. S.; Li, X.; Liu, M.; Bottomley, L. A.; Liu, M. Probing and mapping electrode surfaces in solid oxide fuel cells. *J. Visualized Exp.* **2012**, No. e50161.
(42) Li, X.; Blinn, K.; Chen, D.; Liu, M. In Situ and Surface-Enhanced Raman Spectroscopy Study of Electrode Materials in Solid Oxide Fuel Cells. *Electrochem. Energy Rev.* **2018**, *1*, 433−459.
(43) Dong, J.-C.; Zhang, X.-G.; Briega-Martos, V.; Jin, X.; Yang, J.; Chen, S.; Yang, Z.-L.; Wu, D.-Y.; Feliu, J. M.; Williams, C. T.; Tian, Z.-Q.; Li, J.-F. In situ Raman spectroscopic evidence for oxygen reduction reaction intermediates at platinum single-crystal surfaces. *Nat. Energy* **2019**, *4*, 60−67.
(44) Li, J. F.; Huang, Y. F.; Ding, Y.; Yang, Z. L.; Li, S. B.; Zhou, X. S.; Fan, F. R.; Zhang, W.; Zhou, Z. Y.; Wu, D. Y.; Ren, B.; et al. Shell-isolated nanoparticle-enhanced Raman spectroscopy. *Nature* **2010**, *464*, 392−395.
(45) Whitney, A. V.; Elam, J. W.; Stair, P. C.; Van Duyne, R. P. Toward a thermally robust operando surface-enhanced Raman spectroscopy substrate. *J. Phys. Chem. C* **2007**, *111*, 16827−16832.
(46) Liu, M.; Sun, W.; Li, X.; Feng, S.; Ding, D.; Chen, D.; Liu, M.; Park, H. C. High-performance Ni−BaZr0. 1Ce0. 7Y0. 1Yb0. 1O3− δ (BZCYYb) membranes for hydrogen separation. *Int. J. Hydrogen Energy* **2013**, *38*, 14743−14749.
(47) Schmidt, C.; Seward, T. M. Raman spectroscopic quantification of sulfur species in aqueous fluids: Ratios of relative molar scattering factors of Raman bands of H_2S, HS^-, SO_2, HSO_4^-, SO_4^{2-}, $S_2O_3^{2-}$, S_3^- and H_2O at ambient conditions and information on changes with pressure and temperature. *Chem. Geol.* **2017**, *467*, 64−75.
(48) Ben Mabrouk, K.; Kauffmann, T. H.; Aroui, H.; Fontana, M. D. Raman study of cation effect on sulfate vibration modes in solid state and in aqueous solutions. *J. Raman Spectrosc.* **2013**, *44*, 1603−1608.
(49) Harroun, S. G.; Bergman, J.; Jablonski, E.; Brosseau, C. L. Surface-enhanced Raman spectroscopy analysis of house paint and wallpaper samples from an 18 th century historic property. *Analyst* **2011**, *136*, 3453−3460.
(50) Chen, Y.; Xie, C.; Li, Y.; Song, C.; Bolin, T. B. Sulfur poisoning mechanism of steam reforming catalysts: an X-ray absorption near edge structure (XANES) spectroscopic study. *Phys. Chem. Chem. Phys.* **2010**, *12*, 5707−5711.

DOI: 10.1021/acsami.9b17294
ACS Appl. Mater. Interfaces 2020, 12, 2370−2379

(51) Argyle, M.; Bartholomew, C. Heterogeneous Catalyst Deactivation and Regeneration: A Review. *Catalysts* **2015**, *5*, 145.
(52) Herzberg, G.; Crawford, B. L., Jr. Infrared and Raman spectra of polyatomic molecules. *J. Phys. Chem. A.* **1946**, *50*, 288.
(53) Cheng, Z.; Zha, S.; Aguilar, L.; Wang, D.; Winnick, J.; Liu, M. A Solid Oxide Fuel Cell Running on H2S/ CH4 Fuel Mixtures. *Electrochem. Solid-State Lett.* **2006**, *9*, A31−A33.
(54) Yan, N.; Zanna, S.; Klein, L. H.; Roushanafshar, M.; Amirkhiz, B. S.; Zeng, Y.; Rothenberg, G.; Marcus, P.; Luo, J.-L. The surface evolution of $La_{0.4}Sr_{0.6}TiO_{3+\delta}$ anode in solid oxide fuel cells: Understanding the sulfur-promotion effect. *J. Power Sources* **2017**, *343*, 127−134.
(55) Lutz, H. D.; Eckers, W.; Schneider, G.; Haeuseler, H. Raman and infrared spectra of barium and strontium hydroxides and hydroxide hydrates. *Spectrochim. Acta, Part A* **1981**, *37*, 561−567.
(56) Bandura, A.; Evarestov, R.; Kuruch, D. Hybrid HF−DFT modeling of monolayer water adsorption on (001) surface of cubic BaHfO3 and BaZrO3 crystals. *Surf. Sci.* **2010**, *604*, 1591−1597.
(57) Li, J.; Luo, J.-L.; Chuang, K. T.; Sanger, A. R. Chemical stability of Y-doped Ba (Ce, Zr) O3 perovskites in H2S-containing H2. *Electrochim. Acta* **2008**, *53*, 3701−3707.
(58) Chueh, W. C.; Hao, Y.; Jung, W.; Haile, S. M. High electrochemical activity of the oxide phase in model ceria−Pt and ceria−Ni composite anodes. *Nat. Mater.* **2012**, *11*, 155.

DOI: 10.1021/acsami.9b17294
ACS Appl. Mater. Interfaces 2020, 12, 2370−2379